# Density of states in chromium alloys

R. S. Fishman and V. S. Viswanath
*Solid State Division, P.O. Box 2008, Oak Ridge National Lab, Oak Ridge, Tennessee 37831-6032*
(Received 2 July 1996; revised manuscript received 5 December 1996)

Both the spin- and charge-density waves of Cr alloys have significant effects on the joint density-of-states $\rho(\omega)$ of the nested electron and hole Fermi surfaces below the Néel temperature $T_N$. The random-phase approximation is used to evaluate $\rho(\omega)$ within a three-band model of Cr alloys. In the commensurate phase of the spin-density wave, $\rho(\omega)$ contains a single energy gap $2\Delta$. At zero temperature, $2\Delta$ reaches a maximum value of about 370 meV and spans the Fermi energy, which is shifted upwards by the presence of a charge-density wave (CDW). In the incommensurate phase, $\rho(\omega)$ contains two energy gaps $\Delta_1'$ and $\Delta_1$ above and below midgap states. If the CDW order parameter $\delta$ vanishes, then $\Delta_1'=\Delta_1$ and both reach a maximum of about 130 meV at $T=0$; if $\delta$ is nonzero, then $\Delta_1'<\Delta_1$. A third energy gap $\Delta_2$ includes both the midgap states as well as the smaller gaps $\Delta_1$ and $\Delta_1'$. For pure Cr, $\Delta_2$ reaches a maximum value of about 450 meV at $T=0$. Unlike $\Delta_1$ and $\Delta_1'$, $\Delta_2$ does not vanish at $T_N$ but decreases to about 370 meV. Our results are compared with those obtained earlier from a two-band model in the absence of the CDW. This paper also clarifies the assumptions made by the three-band model and the role of the unpaired holes which reside on the larger of the two nested Fermi surfaces. [S0163-1829(97)06913-0]

## I. INTRODUCTION

The spin-density wave (SDW) in Cr alloys is produced by the Coulomb attraction $U$ between electrons and holes on two nearly nested Fermi surfaces.[1,2] Because the hole Fermi surface $b$ is slightly larger than the electron Fermi surface $a$, the SDW of pure Cr is incommensurate (I) with the bcc lattice and a small fraction of the holes are not paired to electrons. The relative sizes of the two Fermi surfaces and the density of unpaired holes may be controlled by doping. When the mismatch between the two Fermi surfaces is sufficiently small, the commensurate (C) phase of the SDW is stabilized. But the Néel temperature continues to rise[3] until the two nested Fermi surfaces are the same size and the density of unpaired holes is zero. In this work, we describe the effects of the unpaired holes on the density-of-states of Cr alloys in both the C and I phases.

To minimize the condensation free energy[4] on both sides of the nested Fermi surfaces, the ordering wave vectors $\mathbf{Q}_{\pm}'=(\mathbf{G}/2)(1\pm\partial')$ of the SDW lie closer to $\mathbf{G}/2=2\pi\hat{\mathbf{z}}/a$ ($a$ is the lattice constant) than the nesting wave vectors $\mathbf{Q}_{\pm}=(\mathbf{G}/2)(1\pm\partial)$. The mismatch $\partial$ between the $a$ and $b$ Fermi surfaces can be controlled by doping with another transition metal: adding Mn, Fe, Re, or Ru raises the Fermi energy $\epsilon_F$ and decreases the mismatch $\partial$; adding V lowers $\epsilon_F$ and increases $\partial$. For pure Cr, $\partial\approx 0.05$ so that the hole Fermi surface is slightly larger than the electron surface. As $\partial$ decreases and the nesting improves, $\partial'<\partial$ also decreases until, for a small enough mismatch $\partial>0$, the SDW becomes commensurate with the lattice and $\partial'=0$. Although domains of the ISDW may form along any of the three crystal axes, an ISDW along the $z$ axis can be selected by cooling the I alloy in a magnetic field.

In the I phase, the Coulomb attraction $U'$ between the paired electrons and unpaired holes produces a charge-density wave[6,7] (CDW) with twice the wave vector of the SDW. To ensure charge conservation,[8] the CDW must vanish in the C phase. But by shifting the Fermi energy, $U'$ drives the strongly first-order paramagnetic (P) to C transition observed[3] in CrFe and CrSi alloys.

The calculations performed in this paper are based on a three-band model, in which the mismatch on one side of the electron and hole Fermi surfaces directly affects the nesting on the other side. Even in the absence of a CDW, the predictions of the three-band model for the I density-of-states differ from the results[10–12] of a two-band model. The deficiencies of the free energy constructed from a two-band model are well-known: in disagreement with experiments, the two-band model predicts that the PC and PI phase transitions are always second order. A three-band model is also required to produce a sensible description of the I spin dynamics.[5]

But the most glaring deficiency of the two-band model is that it cannot self-consistently describe the effects of a CDW. While a CDW *is* obtained from the two-band model of Machida and Fujita,[11] it does not self-consistently affect the quasiparticle energies or free energy. As will soon be evident, the CDW has a pronounced effect on the density-of-states and energy gaps of the I phase. The role of the CDW in determining the orders of the various phase transitions is presented elsewhere.[8]

The purpose of this paper is twofold. First, we will clarify the physics of the three-band model. Contrary to some expectations,[9] the three-band model does not double the number of quasiparticle states and does lead to quite sensible results for the density-of-states. Second, we will study the effects of a CDW and a finite electron reservoir on the density-of-states of Cr alloys. We shall see that the presence of a CDW and finite reservoir may dramatically change the evolution of the energy gaps across a second-order CI phase transition.

Using the random-phase approximation for the spin and charge distributions, we shall calculate the change in the density-of-states $\Delta\rho(\omega)$ below the Néel temperature. In the I phase, the density-of-states contains two energy gaps $\Delta_1'$ and $\Delta_1$ above and below midgap states. When the CDW order parameter is nonzero, $\Delta_1'<\Delta_1$ but both reach a maximum at zero temperature. A third energy gap $\Delta_2$ straddles both $\Delta_1$

 

and $\Delta_1'$ as well as the midgap states. Unlike $\Delta_1$ and $\Delta_1'$, $\Delta_2$ approaches a nonzero value at the Néel temperature.

This paper is divided into five sections. The Green's-function formalism is presented in Sec. II. Section III contains our results for the density-of-states. Section IV discusses the assumptions underlying the three-band model of Cr alloys. Section V compares our theoretical results for the density-of-states and energy gaps with experiments and with earlier theoretical results based on a two-band model. The spin and charge distributions are derived in the Appendix.

## II. FORMALISM

As in previous work,[4] we assume that the paramagnetic densities-of-states $\rho_{\rm eh}/2$ of the $a$ and $b$ Fermi surfaces are equal and that their Fermi velocities have the same magnitude. These assumptions shall be justified later. Besides the nearly nested Fermi surfaces $a$ and $b$, the band structure of Cr alloys also contains two other bands[13] of electron balls and hole pockets which may be lumped together into an electron reservoir[14] with density-of-states $\rho_r$ and power $p=\rho_r/\rho_{\rm eh}$. If the electron reservoir is finite, then the Fermi energy $\epsilon_F$ will decrease and the mismatch $\partial$ will increase as the SDW grows. So a finite electron reservoir favors the I phase of the SDW. Band-structure calculations[13] indicate that $p$ lies between 1.03 and 4.35, so that the reservoir bands contain at least as many states near the Fermi energy as do the $a$ and $b$ bands.

In Fig. 1(a), the paramagnetic energies of band $b$ are shifted by the ordering wavevectors $\mathbf{Q}_{\pm}'$. These shifted bands are denoted as $b-$ and $b+$. The linearized energies in the boxed region near the Fermi wave vector $k_F$ are then plotted as the dashed lines in Figs. 1(b) and 1(c) for the I and C phases, respectively. In all three figures, the Fermi energy is drawn as a dashed horizontal line and $z=v_F(\mathbf{k}\cdot\hat{\mathbf{n}}-k_F)$ measures the momentum difference from an octahedral face of the electron Fermi surface with normal $\hat{\mathbf{n}}$. The paramagnetic energies are then specified by the parameters $z_0=4\pi\partial v_F/\sqrt{3}a$ and $\kappa=z_0\partial'/2\partial<z_0/2$. For pure Cr, $z_0\approx 600$ meV and $\kappa\approx 300$ meV. Changes in the energy mismatch $z_0$ with doping are linearly related[15] to changes in the Fermi energy $\epsilon_F$ by $\Delta z_0=-4\Delta\epsilon_F$. While the mismatch energy $z_0$ increases linearly with the V concentration, it decreases linearly with the concentration of Mn, Fe, Re, or Ru. The incommensurability energy $\kappa$ approaches $z_0/2$ as $\partial'\to\partial$ and vanishes for a C alloy with $\partial'=0$. Another quantity which will appear shortly is the phenomenological Néel temperature $T_N^*\approx 105$ meV of a perfectly nested Cr alloy with $z_0=0$ and $\kappa=0$. This temperature will be formally defined later in the paper.

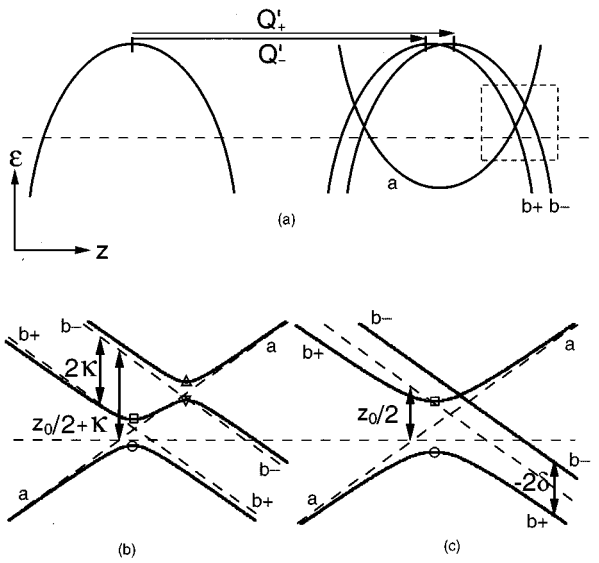


FIG. 1. (a) Electron ($a$) and hole ($b$) energies $\epsilon$ are plotted versus the momentum difference $z$ from an octahedral face of the Fermi surface. The $b$ energies are also translated by the SDW wave vectors $\mathbf{Q}_{\pm}'$. Near the Fermi energy, the boxed region is expanded in (b) and (c) for the I and C phases, respectively. Paramagnetic (short-dashed) and hybridized (solid) quasiparticle energies $\epsilon$ are plotted versus $z$. In all three figures, the Fermi energy is denoted by a horizontal dashed line.

The hybridized quasiparticle energies below the Néel temperature are obtained from the six-dimensional inverse Green's function[8] in band $\{a,b-,b+\}$ and spin space:

$$\underline{G}^{-1}(\mathbf{k},i\nu_l)=\begin{pmatrix} [i\nu_l-\epsilon_a(\mathbf{k})]\underline{1} & -g\hat{\mathbf{m}}\cdot\underline{\boldsymbol{\sigma}}e^{i\phi_-} & -g\hat{\mathbf{m}}\cdot\underline{\boldsymbol{\sigma}}e^{i\phi_+} \\ -g\hat{\mathbf{m}}\cdot\underline{\boldsymbol{\sigma}}e^{-i\phi_-} & [i\nu_l-\epsilon_{b-}(\mathbf{k})]\underline{1} & -\delta\underline{1}e^{i\psi} \\ -g\hat{\mathbf{m}}\cdot\underline{\boldsymbol{\sigma}}e^{-i\phi_+} & -\delta\underline{1}e^{-i\psi} & [i\nu_l-\epsilon_{b+}(\mathbf{k})]\underline{1} \end{pmatrix}, \tag{1}$$

where $\nu_l=(2l+1)\pi T$, $\hat{\mathbf{m}}$ is the polarization direction of the SDW, and $\underline{\boldsymbol{\sigma}}$ are the Pauli matrices in spin space. To ensure that the SDW and CDW order parameters $g$ and $\delta$ are real, the phases $\phi_+$, $\phi_-$, and $\psi$ have been introduced in this inverse Green's function. In the Appendix, we show that the self-consistent relations for the order parameters $g$ and $\delta$ imply that $\psi=\phi_+-\phi_-$. The quasiparticle energies are then obtained from the condition $\mathrm{Det}\underline{G}^{-1}(\mathbf{k},\epsilon)=0$, which may be rewritten as

$$(\epsilon-z)[(\epsilon+z-z_0/2)^2-\kappa^2-\delta^2]-2g^2(\epsilon+z-z_0/2+\delta)=0. \tag{2}$$

The roots $z_i(\epsilon)$ of this cubic equation are labeled so that $z_1\to\epsilon$, $z_2\to-\epsilon+z_0/2-\kappa$, and $z_3\to-\epsilon+z_0/2+\kappa$ as $g\to 0$

and $\delta \to 0$. In the C phase, the roots can be evaluated exactly:

$$z_1 = \frac{z_0}{4} + \frac{\delta}{2} + \sqrt{\left(\epsilon - \frac{z_0}{4} - \frac{\delta}{2}\right)^2 - \Delta^2},$$

$$z_2 = \frac{z_0}{4} + \frac{\delta}{2} - \sqrt{\left(\epsilon - \frac{z_0}{4} - \frac{\delta}{2}\right)^2 - \Delta^2}, \tag{3}$$

$$z_3 = -\epsilon + \frac{z_0}{2} - \delta,$$

where $2\Delta = 2\sqrt{2}g$ is the energy gap joining the circular and square points in Fig. 1(c). In the I phase, the roots $z_i$ must be evaluated numerically.

Below the Néel temperature, the paramagnetic indices $b\pm$ and $a$ are used to label the three hybridized bands. For the I energies sketched in Fig. 1(b), the lower and upper bands are denoted as the $ab+$ and $ab-$ bands, respectively. In the limit $|z| \to \infty$, the right or left branches of the $ab\pm$ bands are displaced from the paramagnetic $b\pm$ energies by the amount $\sqrt{\kappa^2 + \delta^2} - \kappa$. The central $b+b-$ band is similarly displaced from the paramagnetic $b\pm$ energies in this limit. So the crossing of the solid and dashed lines in Fig. 1(b) was not a drafting accident.

For the C phase, the $b+$ and $b-$ energies are identical. However, for reasons that will become clear shortly, the straight band with energy $-z + z_0/2 - \delta$ in Fig. 1(c) is denoted as the $b-$ band. The other two bands will be called the upper and lower $ab+$ bands. As $z \to \pm\infty$, the energy difference between the $b-$ band and the lower or upper $ab+$ bands tends to $2|\delta|$.

In the Appendix, we show that the spin and electron number densities corresponding to the inverse Green's function of Eq. (1) are given by

$$\begin{aligned}\mathbf{S}(\mathbf{r}) &= -\frac{\hbar}{4\lambda} V \rho_{\rm eh} g \hat{\mathbf{m}} |u(\mathbf{r})|^2 \{\cos(\mathbf{Q}'_+ \cdot \mathbf{r} - \phi_+) \\ &\quad + \cos(\mathbf{Q}'_- \cdot \mathbf{r} - \phi_-)\} \\ &= -\frac{\hbar}{2\lambda} V \rho_{\rm eh} g \hat{\mathbf{m}} |u(\mathbf{r})|^2 \cos\left(\frac{2\pi}{a} r_z - \phi_{\rm av}\right) \\ &\quad \times \cos\left(\frac{2\pi}{a} \partial' r_z - \frac{\theta}{2}\right),\end{aligned} \tag{4}$$

$$\begin{aligned}\varrho(\mathbf{r}) &= -\frac{1}{2\lambda'} V \rho_{\rm eh} \delta |u(\mathbf{r})|^2 \cos[(\mathbf{Q}'_+ - \mathbf{Q}'_-) \cdot \mathbf{r} - \phi_+ + \phi_-] \\ &= -\frac{1}{2\lambda'} V \rho_{\rm eh} \delta |u(\mathbf{r})|^2 \cos\left(\frac{4\pi}{a} \partial' r_z - \theta\right),\end{aligned} \tag{5}$$

where $\lambda = U\rho_{\rm eh}/8$ and $\lambda' = U'\rho_{\rm eh}/8$ are dimensionless Coulomb constants. The average phase and the phase difference of the two ISDW's are defined by $\phi_{\rm av} = (\phi_+ + \phi_-)/2$ and $\theta = \phi_+ - \phi_-$. Finally, $u(\mathbf{r})$ is a periodic Bloch function normalized to 1 in volume $V$. Because the Bloch functions of the $d$-band electrons are strongly peaked at the atomic sites, the maximum values of the spin and electron number at each of the $N$ sites in the I phase are approximately $S_0 = -(\hbar g/2\lambda)\cos\phi_{\rm av}(V/N)\rho_{\rm eh}$ and $\varrho_0 = -(\delta/2\lambda')(V/N)\rho_{\rm eh}$.

Both the order parameters $g$ and $\delta$ and the wave-vector parameter $\kappa$ are obtained by minimizing the free-energy difference[8] $\Delta F(p,T)$ between the paramagnetic and ordered states. The reservoir power $p$ affects[15] $\Delta F(p,T)$ by shifting the Fermi energy in order to conserve particle number. For an infinite reservoir, the Fermi energy and energy mismatch $z_0(p=\infty)$ do not change with temperature. But for a finite reservoir, the Fermi energy must decrease and the energy mismatch $z_0(p,T)$ must increase with decreasing temperature. So for a fixed temperature and paramagnetic mismatch energy $z_0(p, T > T_N)$, the order parameters and wave vector depend on the power of the electron reservoir. Within the three-band model, the reservoir power then determines the orders of the different phase transitions: when $p$ is greater than about 2, the CI transition becomes first order as observed in CrMn alloys. By contrast, the CI transition within the two-band model[11] is found to be second order for all values of the reservoir power. In the following discussion, $z_0$ shall denote the temperature-dependent mismatch energy $z_0(p,T)$ except where noted.

The size of the CDW order parameter[8] $\delta < 0$ is determined by the coupling constant $\lambda'$, which ranges from 0 to 1/2. In the limit $\lambda' \to 0$, the CDW order parameter $\delta$ vanishes but the CDW amplitude $\varrho_0 \propto -\delta/\lambda'$ approaches a nonzero value. With increasing $\lambda'$, the triple point shifts to larger values of $z_0$ and the C phase dominates the phase diagram. As $\lambda' \to 1/2$, $\delta \to -z_0/2$ and the C phase is stable for all mismatch energies $z_0$. For the C phase with $\partial' = 0$, conservation of electron number[8] requires that $\varrho(\mathbf{r}) = 0$ or that $\cos\theta = 0$. This relation also guarantees that, while the rms spin is continuous, the SDW amplitude drops from $S_0$ to $S_0/\sqrt{2}$ across a second-order IC phase boundary. Since the CDW order parameter $\delta$ is created by the Coulomb attraction between unpaired holes and paired electrons, $\delta$ vanishes when the electron and hole Fermi surfaces are perfectly nested with $z_0 = 0$.

Fenton and Leavens[9] have argued the three-band model is unphysical because it increases the number of quasiparticle states below the Néel temperature. We emphasize that the three-band model may only be used to evaluate the *changes* produced by the magnetic and charge ordering below $T_N$. So the three bands of quasiparticle energies in Figs. 1(b) and 1(c) do *not* imply that the quasiparticle states on all three bands may be occupied. Rather, the three bands of quasiparticle energies can be used to study the redistribution of quasiparticle states below $T_N$. As we shall see, the change in the density-of-states does not create any new quasiparticle states below $T_N$: instead the possible quasiparticle states are redistributed by the formation of the SDW and CDW.

Many physically important effects are associated with the redistribution of the excess holes on the larger $b$ Fermi surface. Since the mismatch between the paramagnetic C energies of Fig. 1(c) is $z_0/2$, the density of excess holes is $z_0\rho_{\rm eh}/4$. The same density can be extracted from the paramagnetic I energies of Fig. 1(b): if one side of the Fermi surface is perfectly nested with $\kappa = z_0/2$, then all of the excess holes would reside on the other side with mismatch $z_0/2 + \kappa = z_0$.

Below the Néel temperature, the three-band model can be used to study the redistribution of the excess holes. The straight $b-$ band in Fig. 1(c) is displaced from its paramagnetic value solely by the CDW order parameter $\delta$. When $\delta=0$, all of the excess holes are accounted for in the lower $ab+$ band so that the $b-$ band is empty. But as $\lambda'$ and $-\delta$ increase, the unpaired holes migrate to the $b-$ band, which shifts upwards as the $ab+$ bands shift downwards. In the limit $\lambda'\to 1/2$, $\delta\to -z_0/2$, all of the unpaired holes reside on the $b-$ band, and the $ab+$ bands lie symmetrically on either side of the Fermi energy.

For the I energies plotted in Fig. 1(b) with $\kappa<z_0/2$, some of the excess holes must reside on the central $b+b-$ band even when $\lambda'=0$. As $\lambda'$ and $-\delta$ increase, electrons transfer from the $b-$ band to the $ab+$ band. Simultaneously, holes migrate from the $ab+$ band to the upper bands and the $ab+$ band moves downwards. The CDW of Eq. (5) is produced by the Coulomb attraction $U'$ between paired electrons on the lower band and unpaired holes on the upper bands.

Unlike the three bands of quasiparticle states, the joint density-of-states $\rho(\omega)$ of the nested Fermi surfaces may be directly measured. As mentioned in the Introduction, the density-of-states has never been evaluated for the I phase within a three-band model, even in the absence of a CDW. The change in the density-of-states from its paramagnetic value $\rho_{\rm eh}$ is formally given by[16]

$$\Delta\rho(\omega)=\Delta\rho_a(\omega)+\Delta\rho_b(\omega), \tag{6}$$

$$\Delta\rho_a(\omega)=-\frac{1}{2\pi}\rho_{\rm eh}{\rm Im}\int dz\left\{G^{\uparrow\uparrow}_{aa}(\mathbf{k},\omega+i\xi)-\frac{1}{\omega-z+i\xi}\right\}, \tag{7}$$

$$\Delta\rho_b(\omega)=-\frac{1}{2\pi}\rho_{\rm eh}{\rm Im}\int dz\left\{G^{\uparrow\uparrow}_{b+b+}(\mathbf{k},\omega+i\xi)+G^{\uparrow\uparrow}_{b-b-}(\mathbf{k},\omega+i\xi)-\frac{1}{\omega+z-z_0/2-\kappa+i\xi}-\frac{1}{\omega+z-z_0/2+\kappa+i\xi}\right\} \tag{8}$$

which must be evaluated as $\xi\to 0^+$. Due to their spin symmetries, the matrix elements $\underline{G}_{ab\pm}(\mathbf{k},\omega)\propto\hat{\mathbf{m}}\cdot\underline{\sigma}$ do not contribute to the density-of-states. The summed density-of-states of the $\underline{G}_{b\pm b\mp}(\mathbf{k},\omega)\propto\underline{1}e^{\mp i\theta}$ matrix elements also vanishes: in the I phase because $\mathbf{Q}'_+-\mathbf{Q}'_-\neq 0$ and in the C phase because $\cos\theta=0$.

Of the three roots $z_i(\omega+i\xi)$, only $z_1$ lies in the upper-half plane. So it is straightforward to show that

$$\Delta\rho_a(\omega)=\rho_{\rm eh}{\rm Re}\left\{\frac{(\omega+z_1-z_0/2)^2-\kappa^2-\delta^2}{(z_1-z_2)(z_1-z_3)}-1\right\}, \tag{9}$$

$$\Delta\rho_b(\omega)=2\rho_{\rm eh}{\rm Re}\left\{\frac{(\omega-z_1)(\omega+z_1-z_0/2)-2g^2}{(z_1-z_2)(z_1-z_3)}\right\}. \tag{10}$$

If the paramagnetic parts were not subtracted in Eqs. (7) and (8), then the integrals over $z$ would be undefined. Using Eq. (2) for the roots $z_i$, we find that $\Delta\rho_a(\omega)=\Delta\rho_b(\omega)$ and

$$\rho(\omega)=\rho_{\rm eh}+4\rho_{\rm eh}{\rm Re}\left\{\frac{(\omega-z_1)(\omega+z_1-z_0/2)-2g^2}{(z_1-z_2)(z_1-z_3)}\right\}, \tag{11}$$

which now includes the paramagnetic density-of-states $\rho_{\rm eh}$.

In the C phase, the exact solutions of Eq. (3) can be used to explicitly evaluate the density-of-states of the nested bands:

$$\rho(\omega)=\rho_{\rm eh}{\rm Re}\left\{\frac{\omega'\,{\rm sgn}(\omega')}{\sqrt{\omega'^2-\Delta^2}}\right\}, \tag{12}$$

$$\omega'=\omega-\frac{z_0}{4}-\frac{\delta}{2}. \tag{13}$$

Except for the shift in the Fermi energy, this is identical to the result[16] for a BCS superconductor. For the case of perfect nesting with $z_0=0$ and $\delta=0$, this relationship was first derived by Fedders and Martin.[2] Generally, the Fermi energy at $\omega=0$ lies $z_0/4+\delta/2>0$ below the midpoint of the energy gap at $\omega'=0$. As $\lambda'$ increases from 0 to 1/2, the CDW order parameter $-\delta$ grows from 0 to $z_0/2$. For $\lambda'<1/2$, some of the unpaired holes reside on the $ab+$ bands so that the Fermi energy lies below the midpoint of the gap. In the limit $\lambda'\to 1/2$, all of the unpaired holes have migrated to the $b-$ band so the Fermi energy lies in the middle of the gap.

For either the C or I phases, it can be shown that

$$\int_{-\infty}^{\infty}d\omega\,\Delta\rho(\omega)=0, \tag{14}$$

so the joint density-of-states simply redistributes the quasiparticle states below the Néel temperature but does not create any new ones. In the C phase, Eq. (14) can be demonstrated analytically; in the I phase, it can be shown numerically.

## III. DENSITY-OF-STATES

To demonstrate the correspondence between the quasiparticle energies and the density-of-states, we start with the simplest case $\lambda'=0$ and $\delta=0$. The quasiparticle energies for four different sets of $\{z_0,g,\kappa\}$ are plotted in Figs. 2(a)–2(d). In all four figures, the Fermi energy is drawn as a dashed horizontal line. The values for $g$ and $\kappa$ were obtained at zero temperature. So the lower $ab+$ band always lies completely below the Fermi energy. The corresponding densities-of-states are plotted in Figs. 3(a)–3(d).

For the C case in Fig. 2(a), the Fermi energy lies $z_0/4=1.1T_N^*$ below the midpoint of the energy gap $2\Delta\approx 3.53T_N^*$ between the $ab+$ bands. When $\delta=0$, all of the unpaired holes reside on the $ab+$ bands and the straight central $b-$ band is empty. Notice that the density-of-states in Fig. 3(a) shows no sign of the $b-$ band.

With the same mismatch energy $z_0$, an I set of solutions for $\{g,\kappa\}$ is used to plot the quasiparticle energies and density-of-states in Figs. 2(b) and 3(b). Now the unpaired holes are distributed among all three bands and two gaps of the same size $\Delta_1$ appear above and below the central band. Correspondingly, $\rho(\omega)$ contains midgap states between the $ab+$ and $ab-$ bands. Unlike the C energy gap, the energy gaps above and below the central $b+b-$ band are not per-

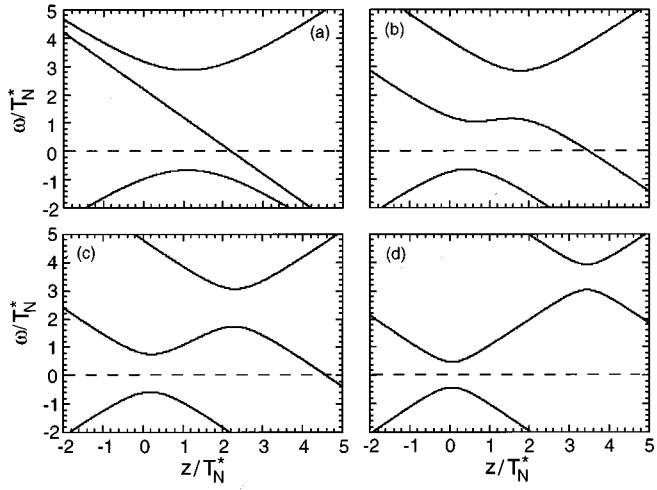


FIG. 2. The hybridized quasiparticle energies $\omega$ versus momentum $z$ for (a) $z_0=4.4T_N^*$, $g=1.247T_N^*$, and $\kappa=0$, (b) $z_0=4.4T_N^*$, $g=0.893T_N^*$, and $\kappa=1.497T_N^*$, (c) $z_0=5T_N^*$, $g=0.676T_N^*$, and $\kappa=2.2T_N^*$, and (d) $z_0=7T_N^*$, $g=0.452T_N^*$, and $\kappa=3.411T_N^*$. All figures take $\delta=0$.

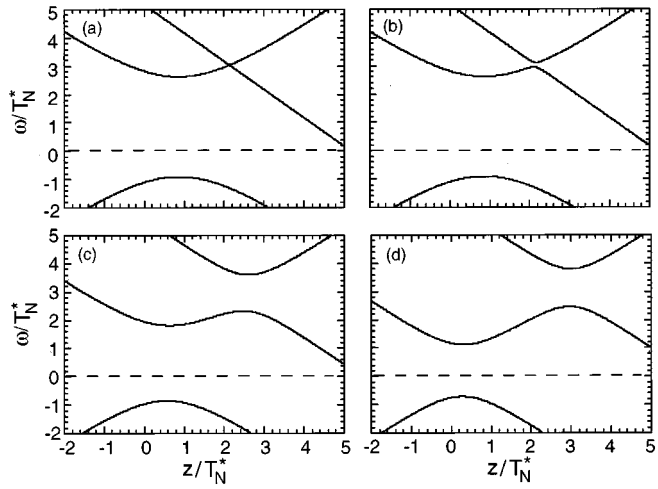


FIG. 4. The hybridized quasiparticle energies $\omega$ versus momentum $z$ for (a) $z_0=6.89T_N^*$, $g=1.247T_N^*$, $\delta=-1.723T_N^*$, and $\kappa=0$, (b) $z_0=6.88T_N^*$, $g=1.246T_N^*$, $\delta=-1.717T_N^*$, and $\kappa=0.179T_N^*$, (c) $z_0=6.6T_N^*$, $g=1.0631T_N^*$, $\delta=-1.346T_N^*$, and $\kappa=1.768T_N^*$, and (d) $z_0=6.6T_N^*$, $g=0.807T_N^*$, $\delta=-0.858T_N^*$, and $\kappa=2.673T_N^*$. These values were obtained with $\lambda'=0.4$.

fect: as clearly shown in Fig. 3(b), quasiparticle states lie within each gap.

While the lower gap $\Delta_1$ corresponds to the energy difference between the circular and square points in Fig. 1(b), the upper gap corresponds to the energy difference between the inverted triangular and triangular points. In Fig. 3(c), $\Delta_2$ is defined to include both the lower and upper gaps as well as the midgap states between them. The midgap peaks in the density-of-states in Figs. 3(c) and 3(d) [also in Fig. 3(b) but too close together to be seen] correspond to the square and inverted triangular points in Fig. 1(b). As the SDW order parameter decreases in Figs. 2(c) and 2(d), $\Delta_1$ shrinks and the midgap peaks move further apart. Simultaneously, the number of states within each gap decreases.

The results of a two-band model[10–12] for the density-of-states are quite similar to those in Figs. 3(b)–3(d) except that no states lie within the gaps. We shall return to the differences between the two- and three-band models below. Within a local spin-density formalism, Hirai[17] also obtained a density-of-states with two energy gaps near the Fermi energy.

Despite appearances, the quasiparticle transition across $\Delta_1$ involves a small change in momentum. As can be shown analytically, the square in Fig. 1(b) lies at a slightly higher value of $z$ than the circle. Of course, the transition across $\Delta_2$ between the circular and triangular points in Fig. 1(b) is quite indirect, involving a momentum change of about $\partial'\mathbf{G}\approx 0.05\mathbf{G}$. At zero-temperature, $\Delta_2(0)$ is larger than the C gap $2\Delta(0)$ and approaches $2\Delta(0)$ as $\kappa\to 0$.

The quasiparticle energies and densities-of-states are significantly altered when the CDW order parameter $\delta$ is nonzero. For the C phase plotted in Figs. 4(a) and 5(a), the straight central $b-$ band again does not contribute to the density-of-states between the $ab+$ bands. Since the $b-$

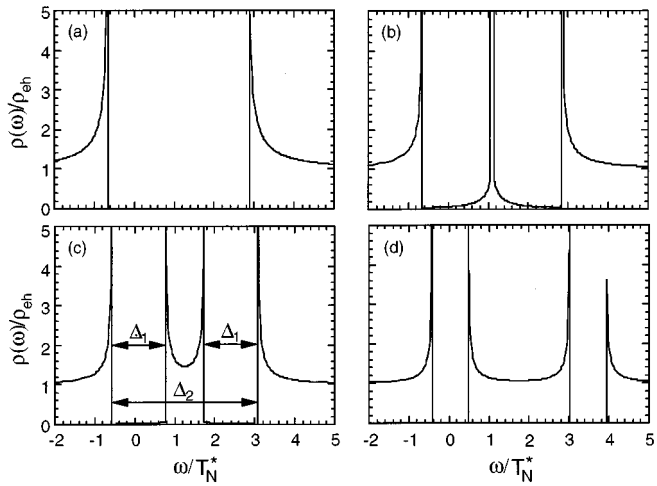


FIG. 3. The density-of-states $\rho(\omega)$ versus frequency $\omega$ for the same values as in Fig. 2.

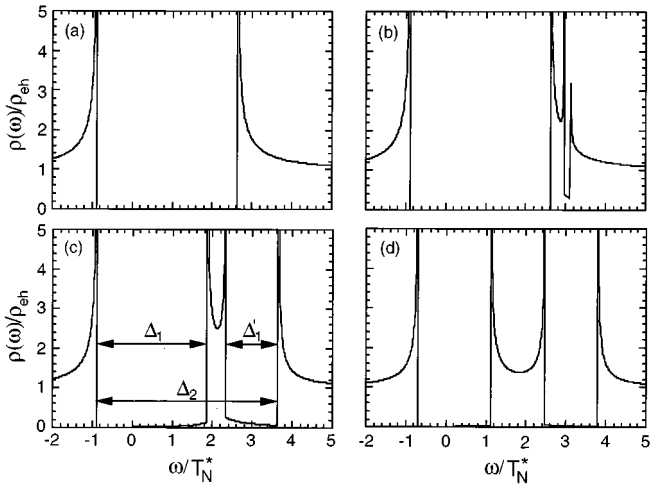


FIG. 5. The density-of-states $\rho(\omega)$ versus frequency $\omega$ for the same values as in Fig. 4.

band contains $-\rho_{\rm eh}\delta/2$ of the excess holes, this result may be surprising. But as discussed below, the contribution of the unpaired holes on the $b-$ band to the joint density-of-states $\rho(\omega)$ is negligibly small on the scale of $\rho_{\rm eh}$.

When $-\delta>0$, the I gap $\Delta_1'$ above the midgap states is smaller than the gap $\Delta_1$ below. To demonstrate the development of the upper energy gap when $\lambda'>0$, we use unstable solutions $\{g,\delta,\kappa\}$ of the free energy $\Delta F(p=\infty)$ in Figs. 4(b), 4(c), 5(b), and 5(c). When the reservoir density-of-states $p\rho_{\rm eh}$ is sufficiently small, these unstable solutions become the stable minima of $\Delta F(p)$. Following the scenario in Figs. 4(b)–4(d) and Figs. 5(b)–5(d), the upper energy gap $\Delta_1'$ develops from zero and initially contains quite a large number of quasiparticle states. As $\kappa$ increases, the number of states inside $\Delta_1'$ diminishes but $\Delta_1'$ always remains smaller than $\Delta_1$ for any $-\delta>0$.

In addition to the quasiparticle states of the nested $a$ and $b$ Fermi surfaces, the total density-of-states of Cr alloys must also include the quasiparticle states of the non-nested reservoir bands.[13] So the total density-of-states should be written as

$$\rho_t(\omega)=\rho(\omega)+p\rho_{\rm eh}. \tag{15}$$

Consequently, all the gaps in Figs. 3 and 5 will contain large numbers of reservoir states. In the limits $\omega/T_N^*\rightarrow\pm\infty$, the total density-of-states $\rho_t(\omega)$ approaches $(1+p)\rho_{\rm eh}$.

As the temperature decreases below $T_N$, the conductivity[18] of the electrons on the nested Fermi surfaces drops but the conductivity of the electrons on the reservoir bands is unaffected. While the resisitivity of most Cr alloys is continuous at $T_N$, the resistivity of $Cr_{1-x}Fe_x$ $(x=0.03)$ increases dramatically[18] due to the sudden formation of a large energy gap at the first-order PC transition.

## IV. PHYSICS OF THE THREE-BAND MODEL

Formally, the straight $b-$ bands in Figs. 2(a) and 4(a) do not contribute to $\rho(\omega)$ because the paramagnetic density-of-states contains $a$, $b-$, and $b+$ bands. So the absence of both $a$ and $b+$ bands inside the C energy gap implies that $\Delta\rho_a(\omega)=-\rho_{\rm eh}/2$ and $\Delta\rho_b(\omega)=-\rho_{\rm eh}/2$ or that $\Delta\rho(\omega)=-\rho_{\rm eh}$ and $\rho(\omega)=0$.

But we have also argued that in the C phase, the $b-$ band contains a density $-\delta\rho_{\rm eh}/2$ of unpaired holes. To physically explain the absence of those unpaired holes from the C density-of-states in Fig. 4(a), we must reexamine the assumptions made by the three-band model. Just as in Fermi-liquid theory, our model of itinerant antiferromagnetism assumes that quasiparticle states are only defined within a range $\epsilon_0$ of the Fermi surface. This energy regulates a logarithmically divergent integral in the self-consistent equation for $g$ given by Eq. (A1). In both this self-consistent equation and in the free-energy difference $\Delta F(p,T)$, the cutoff $\epsilon_0$ may be replaced by the phenomenological Néel temperature

$$T_N^*=1.13\epsilon_0 e^{-1/2\lambda} \tag{16}$$

of a perfectly nested alloy with $z_0=0$. In the BCS theory of conventional superconductivity, the Debye frequency $\omega_D$ replaces the energy cutoff $\epsilon_0$. Hence, itinerant models of antiferromagnetism more closely resemble the weak-coupling theory[16] of superfluid $He^3$, in which the cutoff $\epsilon_0$ also has no direct physical significance. As in the BCS theory of $He^3$, $\epsilon_0$ is assumed to obey the relationship

$$X\ll\epsilon_0\ll\epsilon_F, \tag{17}$$

where $X$ stands for all other energy scales: $T_N^*$, $g$, $-\delta$, or $z_0$. In practice, the energy mismatch $z_0$ may barely satisfy the first inequality: for pure Cr, $z_0\approx 475$ meV and $\epsilon_F\approx 8$ eV, so that less than two orders of magnitude separate these energies.

Due to the assumed separation of energy scales, the energy cutoff $\epsilon_0$ and Coulomb constant $\lambda$ can almost always be absorbed into the phenomenological Néel temperature $T_N^*$. One of the few exceptions to this rule involves the spin density itself. As revealed by Eq. (4), the SDW amplitude $S_0\propto g\cos\phi_{\rm av}/\lambda$ explicitly depends on the Coulomb constant. Since the average phase $\phi_{\rm av}$ is undetermined by the nesting free energy, fitting $S_0$ to the observed SDW amplitude can only establish the maximum value for $\lambda$ or the minimum value for $\epsilon_0$. Depending on the paramagnetic density-of-states[13] $\rho_{\rm eh}$, such a procedure yields a maximum value for $\lambda$ between 0.020 and 0.032, corresponding to astronomically large values of $\epsilon_0$. More reasonable values of $\lambda$ between 0.21 and 0.16 would correspond to $\epsilon_0$ between 1 and 2 eV, the same order as the $d$-band width.[13] The anomalously small value of $\lambda$ may reveal one of the weaknesses of the weak-coupling theory of itinerant antiferromagnetism.

Several postulates of our model are justified by the separation of energy scales. Since the energy mismatch between the $a$ and $b$ Fermi surfaces equals $z_0$, the paramagnetic densities-of-states of the two Fermi surfaces may differ by an amount of order $\rho_{\rm eh}z_0/\epsilon_F$. Due to the inequality $z_0\ll\epsilon_F$, it is certainly justified to assume that the density-of-states $\rho_{\rm eh}$ is equally split between the two Fermi surfaces above $T_N$. It is likewise justified to assume that their Fermi velocities have the same magnitude.

Because $-\delta\ll\epsilon_F$, the density $-\delta\rho_{\rm eh}/2$ of unpaired holes on the $b-$ band in the C phase is much too small to affect the joint density-of-states $\rho(\omega)$ of the nested Fermi surfaces. Like the quasiparticle states in the reservoir band, the quasiparticle states in the $b-$ band simply add a (negligibly small) constant term to the total $\rho_t(\omega)$ in Eq. (15). Nevertheless, the magnetic properties of Cr alloys are quite sensitive to small changes near the Fermi energy. So the redistribution of unpaired holes has important physical consequences below the Néel temperature. In the I phase, the Coulomb attraction $U'$ between paired holes and unpaired electrons produces the CDW of Eq. (5). In the C phase, this Coulomb interaction shifts the Fermi energy upwards and drives the first-order PC transition observed[3] in CrFe and CrSi alloys.

## V. DISCUSSION AND CONCLUSION

Many experimentalists have used reflectance[19–22] or absorption[18,23,24] measurements to study the energy gaps of Cr alloys. For C alloys at low temperatures,[18,22–24] $2\Delta$ lies between 360 and 400 meV. Fitting this value to the zero-temperature result $2\Delta(0)=2\sqrt{2}g_0\approx 3.53T_N^*$, we find that $T_N^*$ lies between 102 and 113 meV. Due to impurity scatter-

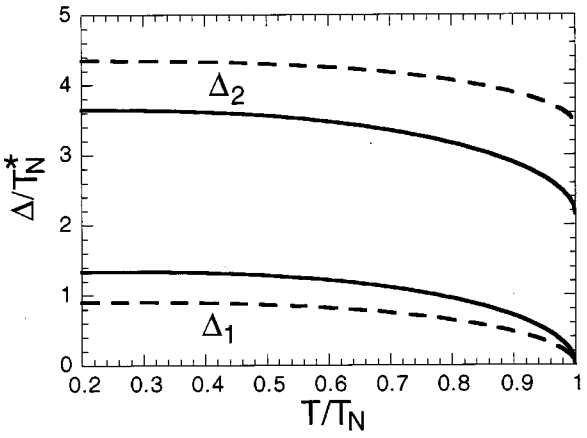


FIG. 6. The energy gaps $\Delta_1$ and $\Delta_2$ versus normalized temperature $T/T_N$ for $\lambda'=0$, $p=\infty$, and $z_0=5T_N^*$ (solid) or $z_0=7T_N^*$ (dashed).

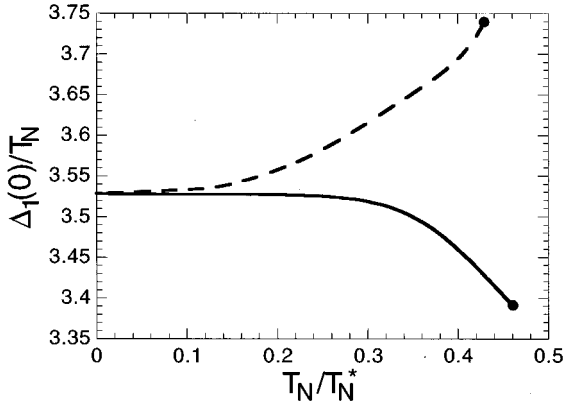


FIG. 8. The normalized energy gap $\Delta_1/T_N$ versus the scaled Néel temperature $T_N/T_N^*$ at $T=0$ with $p=\infty$ and $\lambda'=0$ (solid) or $\lambda'=0.10$ (dashed).

ing, however, this may underestimate $T_N^*$.

For pure Cr at low temperatures,[20] $\Delta_1\approx 124$ meV and $\Delta_2\approx 450$ meV. Whereas $\Delta_1$ is quite flat below about 260 K, $\Delta_2$ is reduced[12] by about 30% to 320 meV at 300 K. A simple analysis of the paramagnetic energies in Fig. 1(b) reveals that $\Delta_2\rightarrow\kappa$ as $T\rightarrow T_N$. The order parameters and wave vectors in Fig. 6 are evaluated with $\lambda'=0$ and $p=\infty$. When $z_0=5T_N^*$, $\Delta_2$ decreases by about 41% between $T=0$ and $T_N$. When $z_0=7T_N^*$, $\Delta_2$ decreases by only 22%. With $z_0=5.7T_N^*$ both zero-temperature gaps $\Delta_1(0)\approx 130$ meV and $\Delta_2(0)\approx 445$ meV are close to the observed values for pure Cr if $T_N^*=115$ meV. For these values, $\Delta_2$ is predicted to decrease by about 31% to $\kappa\approx 305$ meV at $T_N$.

When $\lambda'>0$ and $-\delta>0$, $\rho(\omega)$ is characterized by three inequivalent energy gaps which are plotted versus temperature in Fig. 7 for $\lambda'=0.40$ and $z_0=6.6T_N^*$. The order parameters and wave vector are again evaluated under the condition that $p=\infty$. Now $\Delta_1>\Delta_1'$ but both gaps vanish at $T_N$.

Absorption studies by Barker and Ditzenberger[18] suggest that $\Delta_1(0)$ scales roughly as the Néel temperature $T_N$. Note that both $\Delta_1(0)$ and $T_N$ depend on the mismatch energy $z_0$. To test the scaling of $\Delta_1(0)$ with $T_N$, we plot $\Delta_1(0)/T_N$ versus $T_N/T_N^*$ in Fig. 8, again using $p=\infty$. Since the SDW is enhanced by the presence of a CDW, the normalized energy gap $\Delta_1(0)/T_N$ increases with $\lambda'$. But for either $\lambda'=0$ or $\lambda'=0.10$, $\Delta_1(0)/T_N$ approaches the BCS value $2\pi/\gamma\approx 3.528$ as the Néel temperature vanishes or as the mismatch energy diverges. While $\Delta_1(0)/T_N$ is a decreasing function of the Néel temperature when $\lambda'=0$, this ratio increases with $T_N$ when $\lambda'=0.10$. When $\lambda'=0$, $\Delta_1(0)/T_N$ decreases by only about 4% at the triple point.

In agreement with our results for $\lambda'=0$, the observed energy gaps[18] $\Delta_1$ of CrMn and CrRu alloys fall slightly below the straight line $\alpha T_N$ close to the IC phase boundary. But in disagreement with Fig. 8, the observed slope $\alpha\approx 5.1$ is significantly larger than our estimate of 3.5. Several explanations[18,23,25] have been proposed for this discrepancy. A two-band model predicts values for $\alpha$ either smaller[25] or larger[26] than 3.5. However, the two-band model with its single energy gap is only appropriate in the C phase of Cr alloys (and even then only if the Fermi energy is suitably shifted by the CDW order parameter).

A more likely explanation for the large value for $\alpha$ was originally proposed by Barker, Halperin, and Rice.[19] Impu-

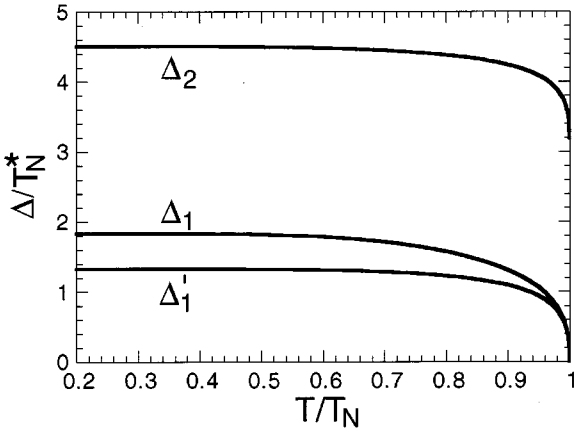


FIG. 7. The energy gaps $\Delta_1$, $\Delta_1'$, and $\Delta_2$ versus $T/T_N$ for $\lambda'=0.4$, $z_0=6.6T_N^*$, and $p=\infty$.

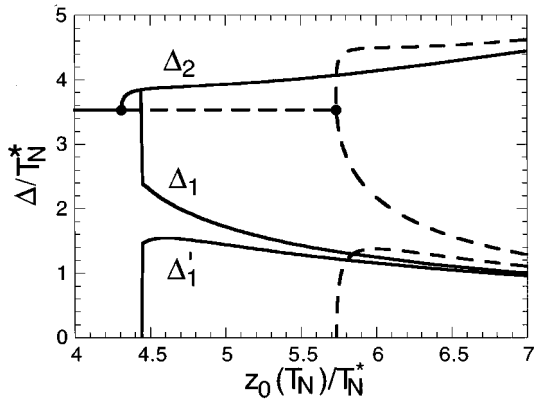


FIG. 9. The energy gaps $\Delta_1$, $\Delta_1'$, and $\Delta_2$ versus the normalized energy mismatch $z_0(T_N)/T_N^*$ for $\lambda'=0.3$ (solid) and 0.4 (dashed) with $T=0$ and $p=2$.

rity and electron-phonon scattering[27] suppress both the energy gap $\Delta_1$ and the Néel temperature $T_N$. At low temperatures, the energy gap $\Delta_1$ is affected primarily by impurity scattering. But the Néel temperature of Cr alloys is strongly suppressed by both impurity and electron-phonon scattering. Hence, the ratio $\Delta_1(0)/T_N$ will be larger than the values indicated by Fig. 8. If electron-phonon scattering dominates over impurity scattering and the scattering rate $\Gamma$ is proportional to $T$, then the modified Néel temperature $\widetilde{T}_N = T_N - \alpha'\Gamma$ will be proportional to $T_N$ and the gap $\Delta_1(0)$ will again scale with $\widetilde{T}_N$.

The energy gaps can be controlled by changing the energy mismatch with doping. As $z_0$ increases with V doping, $\Delta_1$ should decrease while the midgap states and $\Delta_2$ grow. As $z_0$ decreases with Mn or Fe doping, $\Delta_1$ should increase while the midgap states shrink. When $U'=0$ and the CDW is absent, the energy gaps $\Delta_1$ and $\Delta_1'$ change suddenly as a kink develops in the central $b+b-$ band, even if the CI transition is second order. This is still the case for a small CDW. But if $U'$ is sufficiently large that the C $b-$ branch crosses the upper $ab+$ branch to the right of its minimum value, as pictured in Fig. 1(c), then the energy gaps $\Delta_1$ and $\Delta_1'$ will evolve continuously across a second-order CI transition.

These two different scenarios are demonstrated in Fig. 9, where the reservoir power $p=2$ is small enough to produce a second-order CI transition at zero-temperature. The paramagnetic energy mismatch $z_0(T_N)$ here depends only on the impurity concentration and not on the reservoir power. For both $\lambda'=0.3$ and 0.4, the CI transition at $z_0^{\rm CI}(T_N)$ is denoted by a filled circle. To the left of the CI transition, the single energy gap is given by the C value of $2\Delta(0)\approx 3.53T_N^*$.

When the CDW is sufficiently large, such as for $\lambda'=0.4$, the gaps $\Delta_1(0)$ and $\Delta_1'(0)$ are continuous. In this case, $\Delta_1'(0)$ vanishes and $\Delta_1(0)$ approaches $2\Delta(0)$ at the CI phase boundary. Since the midgap states suddenly appear at the CI phase boundary, $\Delta_2(0)$ approaches a C value greater than $2\Delta(0)$. When $\lambda'=0.3$, $\Delta_1(0)$ briefly exceeds $2\Delta(0)$ following the CI transition but prior to a discontinuous change in both $\Delta_1(0)$ and $\Delta_1'(0)$. In the small window of dopant concentrations with $4.31<z_0(T_N)/T_N^*<4.45$, the SDW is incommensurate but only one large energy gap $\Delta_1(0)\approx 2\Delta(0)$ is seen. *The discontinuous changes in the energy gaps occur inside the I phase* with $z_0(T_N) > z_0^{\rm CI}(T_N)=4.31T_N^*$. This remains the case for all smaller values of $\lambda'$ including $\lambda'=0$. In fact, the separation between $z_0^{\rm CI}(T_N)$ and the $z_0(T_N)$ which marks the jumps in the energy gaps *increases* with decreasing $\lambda'$. For $\lambda'=0$, $\Delta_1(0)$ is slightly less than $2\Delta(0)$ within this window. Practically all Cr alloys with modest values of $\lambda'$ (the only possible exception being CrFe alloys) should obey this second scenario.

To test the possibility that the jumps in the energy gaps do *not* coincide with the CI transition, optical measurements should be performed on an I alloy which according to neutron-scattering measurements is close to a second-order or very weakly first-order CI phase boundary. One possibility is to cool a $Cr_{1-x}Mn_x$ alloys with $0.003\leqslant x\leqslant 0.01$ to just below its CI phase boundary. Optical measurements on such an alloy should exhibit a large energy gap close to the C value of 380 meV.

Other techniques have also been used to probe the density-of-states, including angle-resolved photoemission[28] and point-contact spectroscopy.[29] But two recently developed techniques may hold even more promise: inelastic x-ray scattering and electron-energy-loss spectroscopy (EELS). With an energy resolution of 2–4 meV, the latter technique should prove ideal in measuring the temperature dependence of the energy gaps. Since EELS is only sensitive to the Cr surface, however, the energy gaps may be suppressed from their bulk values.

To summarize, we have calculated the density-of-states of Cr alloys using a three-band model within the RPA. The results for the density-of-states have been used to clarify some of the assumptions underlying the three-band model. We have shown that the presence of a CDW and a finite electron reservoir may dramatically alter the evolution of the energy gaps from the C to the I phase of Cr alloys. Observation of the predicted temperature and doping dependence of these energy gaps would provide additional confirmation of the three-band model. We hope that the results presented in this paper will inspire future work in this area of fundamental physical importance.

## ACKNOWLEDGMENTS

We would like to acknowledge support from the U.S. Department of Energy under Contract No. DE-FG06-94ER45519 and under Contract No. DE-AC0586OR22464 with Lockheed Martin Energy Research Corporation. Useful conversations with J. Jellison, J. Tischler, H. Weiterling, and especially with S.H. Liu are also gratefully acknowledged.

## APPENDIX: SPIN AND ELECTRON NUMBER DENSITIES

This appendix generalizes the work of Jiang and Fishman[8] to derive Eqs. (4) and (5) for the spin and electron number densities.

Within the random-phase approximation, the self-consistent relations for the spin and charge-density-wave order parameters are

$$g\hat{\mathbf{m}}\cdot\underline{\vec{\sigma}}\,e^{i\phi_+} = -U\frac{T}{V}\sum_{\mathbf{k},l}\underline{G}^{ab+}(\mathbf{k},i\nu_l), \tag{A1}$$

$$\delta\underline{1}\,e^{i\psi} = -U'\frac{T}{V}\sum_{\mathbf{k},l}\underline{G}^{b-b+}(\mathbf{k},i\nu_l). \tag{A2}$$

These two relations imply that $\psi=\phi_+-\phi_-$ so that the CDW phase equals the difference between the SDW phases. The free-energy difference $\Delta F(p,T)$ is obtained[8] by integrating these self-consistent relations.

The creation and destruction operators for the $d$-band electrons are given in terms of their Bloch functions $u_{\mathbf{k}}(\mathbf{r})$ by

$$\underline{\Psi}(\mathbf{r})=\sum_{\mathbf{k}} e^{-i\mathbf{k}\cdot\mathbf{r}}u_{\mathbf{k}}(\mathbf{r})\begin{pmatrix} a_{\mathbf{k}\uparrow} \\ a_{\mathbf{k}\downarrow} \\ b^{-}_{\mathbf{k}\uparrow} \\ b^{-}_{\mathbf{k}\downarrow} \\ b^{+}_{\mathbf{k}\uparrow} \\ b^{+}_{\mathbf{k}\downarrow} \end{pmatrix}, \tag{A3}$$

$$\underline{\Psi}^{\dagger}(\mathbf{r})=\sum_{\mathbf{k}} e^{i\mathbf{k}\cdot\mathbf{r}}u^{*}_{\mathbf{k}}(\mathbf{r})[a^{\dagger}_{\mathbf{k}\uparrow},a^{\dagger}_{\mathbf{k}\downarrow},b^{-\dagger}_{\mathbf{k}\uparrow},b^{-\dagger}_{\mathbf{k}\downarrow},b^{+\dagger}_{\mathbf{k}\uparrow},b^{+\dagger}_{\mathbf{k}\downarrow}], \tag{A4}$$

where $\Psi(\mathbf{r})$ is a six-dimensional vector in band and spin space and $u_{\mathbf{k}}(\mathbf{r})$ is normalized to one in volume $V$. While $a_{\mathbf{k}\sigma}$ and $a^{\dagger}_{\mathbf{k}\sigma}$ destroy and create electrons on band $a$ with momentum $\mathbf{k}$ and spin $\sigma$, $b^{\pm}_{\mathbf{k}\sigma}$ and $b^{\pm\dagger}_{\mathbf{k}\sigma}$ destroy and create electrons on bands $b_{\pm}$. The spin and charge operators can now be written as

$$S_z(\mathbf{r})=\frac{\hbar}{2}\underline{\Psi}^{\dagger}(\mathbf{r})\begin{pmatrix} \underline{\sigma^z} & \underline{\sigma^z} & \underline{\sigma^z} \\ \underline{\sigma^z} & \underline{\sigma^z} & \underline{\sigma^z} \\ \underline{\sigma^z} & \underline{\sigma^z} & \underline{\sigma^z} \end{pmatrix}\underline{\Psi}(\mathbf{r}), \tag{A5}$$

$$\rho(\mathbf{r})=\underline{\Psi}^{\dagger}(\mathbf{r})\begin{pmatrix} \underline{1} & \underline{1} & \underline{1} \\ \underline{1} & \underline{1} & \underline{1} \\ \underline{1} & \underline{1} & \underline{1} \end{pmatrix}\underline{\Psi}(\mathbf{r}), \tag{A6}$$

where the polarization direction of the spin is taken along the $z$ axis. Note that this axis may differ from the direction of the ordering wave vectors $\mathbf{Q}'_{\pm}$.

Summing repeated spin indices and ignoring the momentum dependence of the Bloch functions, we find that the expectation value of the spin is given by

$$\begin{aligned}\langle S_z(\mathbf{r})\rangle=&\frac{\hbar}{2}|u(\mathbf{r})|^2\sigma^z_{\mu\mu}\sum_{\mathbf{k}}\{\langle a^{\dagger}_{\mathbf{k}\mu}b^{+}_{\mathbf{k}\mu}\rangle e^{-i\mathbf{Q}'_{+}\cdot\mathbf{r}}\\&+\langle a^{\dagger}_{\mathbf{k}\mu}b^{-}_{\mathbf{k}\mu}\rangle e^{-i\mathbf{Q}'_{-}\cdot\mathbf{r}}+\langle b^{+\dagger}_{\mathbf{k}\mu}a_{\mathbf{k}\mu}\rangle e^{i\mathbf{Q}'_{+}\cdot\mathbf{r}}\\&+\langle b^{-\dagger}_{\mathbf{k}\mu}a_{\mathbf{k}\mu}\rangle e^{i\mathbf{Q}'_{-}\cdot\mathbf{r}}\}.\end{aligned} \tag{A7}$$

This can be written in terms of the Green's functions obtained by inverting Eq. (1) as

$$\begin{aligned}\langle S_z(\mathbf{r})\rangle=&\hbar T|u(\mathbf{r})|^2\sum_{\mathbf{k},l}\{G^{ab^{+}}_{\uparrow\uparrow}(\mathbf{k},i\nu_l)e^{-i\mathbf{Q}'_{+}\cdot\mathbf{r}}\\&+G^{ab^{-}}_{\uparrow\uparrow}(\mathbf{k},i\nu_l)e^{-i\mathbf{Q}'_{-}\cdot\mathbf{r}}+G^{b^{+}a}_{\uparrow\uparrow}(\mathbf{k},i\nu_l)e^{i\mathbf{Q}'_{+}\cdot\mathbf{r}}\\&+G^{b^{-}a}_{\uparrow\uparrow}(\mathbf{k},i\nu_l)e^{i\mathbf{Q}'_{-}\cdot\mathbf{r}}\}.\end{aligned} \tag{A8}$$

Using Eq. (A1) we can express the expectation value as

$$\begin{aligned}\langle\mathbf{S}(\mathbf{r})\rangle=&-\frac{\hbar}{8\lambda}V\rho_{\mathrm{eh}}g\hat{\mathbf{m}}|u(\mathbf{r})|^2\{e^{i\phi_{+}-i\mathbf{Q}'_{+}\cdot\mathbf{r}}+e^{i\phi_{-}-i\mathbf{Q}'_{-}\cdot\mathbf{r}}\\&+e^{-i\phi_{+}+i\mathbf{Q}'_{+}\cdot\mathbf{r}}+e^{-i\phi_{-}+i\mathbf{Q}'_{-}\cdot\mathbf{r}}\}\\=&-\frac{\hbar}{4\lambda}V\rho_{\mathrm{eh}}g\hat{\mathbf{m}}|u(\mathbf{r})|^2\{\cos(\mathbf{Q}'_{+}\cdot\mathbf{r}-\phi_{+})\\&+\cos(\mathbf{Q}'_{-}\cdot\mathbf{r}-\phi_{-})\}.\end{aligned} \tag{A9}$$

Choosing the SDW ordering wave vectors to lie along the $z$ axis gives the second line of Eq. (4).

Proceeding along the same lines, Eq. (5) can be derived from the expectation value of the charge operator

$$\begin{aligned}\langle\rho(\mathbf{r})\rangle=&\delta_{\mu\mu}\sum_{\mathbf{k}}\{\langle b^{-\dagger}_{\mathbf{k}\mu}b^{+}_{\mathbf{k}\mu}\rangle e^{-i(\mathbf{Q}'_{+}-\mathbf{Q}'_{-})\cdot\mathbf{r}}\\&+\langle b^{+\dagger}_{\mathbf{k}\mu}b^{-}_{\mathbf{k}\mu}\rangle e^{i(\mathbf{Q}'_{+}-\mathbf{Q}'_{-})\cdot\mathbf{r}}\}\\=&2T\sum_{\mathbf{k},l}\{G^{b^{-}b^{+}}_{\uparrow\uparrow}(\mathbf{k},i\nu_l)e^{-i(\mathbf{Q}'_{+}-\mathbf{Q}'_{-})\cdot\mathbf{r}}\\&+G^{b^{+}b^{-}}_{\uparrow\uparrow}(\mathbf{k},i\nu_l)e^{i(\mathbf{Q}'_{+}-\mathbf{Q}'_{-})\cdot\mathbf{r}}\}\\=&-\frac{1}{2\lambda'}V\rho_{\mathrm{eh}}|u(\mathbf{r})|^2\cos[(\mathbf{Q}'_{+}-\mathbf{Q}'_{-})\cdot\mathbf{r}\\&-(\phi_{+}-\phi_{-})],\end{aligned} \tag{A10}$$

where Eq. (A2) has been used. The second line of Eq. (5) is obtained by again choosing the SDW ordering wave vectors along the $z$ axis.


[1] W.M. Lomer, Proc. Phys. Soc. London **80**, 489 (1962).
[2] P.A. Fedders and P.C. Martin, Phys. Rev. **143**, 8245 (1966).
[3] The properties of Cr alloys are reviewed by E. Fawcett, H.L. Alberts, V.Yu. Galkin, D.R. Noakes, and J.V. Yakhmi, Rev. Mod. Phys. **66**, 26 (1994). In particular, this comprehensive work contains all the references on CrFe and CrSi alloys.
[4] R.S. Fishman and S.H. Liu, Phys. Rev. B **48**, 3820 (1993).
[5] R.S. Fishman and S.H. Liu, Phys. Rev. B **54**, 7252 (1996).
[6] C.Y. Young and J.B. Sokoloff, J. Phys. F **4**, 1304 (1974).
[7] J.P. Hill, G. Hegelsen, and D. Gibbs, Phys. Rev. B **51**, 10 336 (1995).
[8] X.W. Jiang and R.S. Fishman (unpublished).
[9] E.W. Fenton and C.R. Leavens, J. Phys. F **10**, 1853 (1980).
[10] K. Machida, Phys. Rev. B **30**, 418 (1984).
[11] K. Machida and M. Fujita, Phys. Rev. B **30**, 5284 (1984).
[12] K. Machida, M.A. Lind, and J.L. Stanford, J. Phys. Soc. Jpn. **53**, 4020 (1984).
[13] N.I. Kulikov and E.T. Kulatov, J. Phys. F **12**, 2291 (1982) and references therein.
[14] A. Shibatani, K. Motizuki, and T. Nagamiya, Phys. Rev. **177**, 984 (1969).
[15] R.S. Fishman and S.H. Liu, Phys. Rev. B **49**, 3308 (1994).

[16] G.D. Mahan, *Many Particle Physics* (Plenum, New York, 1990).
[17] K. Hirai, J. Phys. Soc. Jpn. **65**, 586 (1996).
[18] A.S. Barker and J.A. Ditzenberger, Phys. Rev. B **1**, 4378 (1970).
[19] A.S. Barker, B.I. Halperin, and T.M. Rice, Phys. Rev. Lett. **20**, 384 (1968).
[20] M.A. Lind and J.L. Stanford, Phys. Lett. **39A**, 5 (1972).
[21] E. Colavita, A. Franciosi, D.W. Lynch, G. Paolucci, and R. Rosei, Phys. Rev. B **27**, 1653 (1983).
[22] M.A. Lind and J.L. Stanford, J. Phys. Soc. Jpn. **53**, 4029 (1984).
[23] L.W. Bos and D.W. Lynch, Phys. Rev. B **2**, 4567 (1970).
[24] D.W. Lynch, R. Rosei, and J.H. Weaver, Phys. Status Solidi A **27**, 515 (1975).
[25] J.C. Kimball and L.M. Falicov, Phys. Rev. Lett. **20**, 1164 (1968).
[26] S.H. Liu, Phys. Lett. **27A**, 493 (1968).
[27] J. Zittartz, Phys. Rev. **164**, 575 (1967).
[28] L.I. Johansson, L.-G. Petersson, K.-F. Berggren, and J.W. Allen, Phys. Rev. B **22**, 3294 (1980).
[29] H. Meekes, Phys. Rev. B **38**, 5924 (1988).